Multimedia Tools and Applications (2019) 78: 10717–10732
https://doi.org/10.1007/s11042-018-6576-2

Single image fog removal algorithm in spatial domain using fractional order anisotropic diffusion

Savita Nandal[1] · **Sanjeev Kumar**[1]

Received: 18 August 2017 / Revised: 16 August 2018 / Accepted: 20 August 2018 /
Published online: 13 September 2018

Abstract
This paper presents a novel image defogging algorithm using fractional-order anisotropic diffusion equation. The proposed algorithm uses the airlight map extracted from the foggy model as the initial image in the anisotropic diffusion process. The iterative diffusion process improves this airlight map. The anisotropic diffusion process is generalized to the order of any real number between $[1,\ 2)$ using the Riemann-Liouville definition of the fractional order derivatives. The formulation of the iterative process is carried out in the spatial domain to have a simple and computationally efficient implementation. Simulation results validate that the proposed algorithm is outperforming over few of the existing algorithms. The comparison study is carried out using different metrics like contrast gain, colorfulness index, contrast-to-noise ratio and visible edges ratio.

Keywords Airlight map · Anisotropic diffusion · Fractional-order partial derivative · Image defogging

1 Introduction

Digital images captured in foggy conditions suffer from poor visibility, colors artifacts and low contrast due to the absorption and scattering of the atmospheric particles. One of the main reasons for poor visibility is the particles/water droplets in the atmosphere. These droplets reflect light which results in degradation of an image of the scene. Poor visibility is an annoying problem as it adversely affects many computer vision applications such as object detection [10, 15], image/video retrieval [9, 13, 14], and remote sensing [3, 7]. In this context, restoration of the digital images degraded due to fog will be of great importance in computer vision.

In this study, we solve this problem using a heat diffusion-based approach. In literature, several models were proposed using diffusion partial differential equation (PDE) for

✉ Savita Nandal
savi4.dma2014@iitr.ac.in

Sanjeev Kumar
malikfma@iitr.ac.in

[1] Department of Mathematics, Indian Institute of Technology Roorkee, Roorkee, 247667, India

denoising of digital images [20, 28, 32]. In all these models, the noise is considered as the discontinuities in the depth data because of image intensity as functions of the relative depth of the object from the camera. Therefore, anisotropic diffusion acts as smooth filtering on the noisy images by preserving the edge details. The factors responsible for the degradation of an image in the presence of fog are the airlight and attenuation. The light reflected from an object is partially absorbed by the particles in the atmosphere and gets attenuated and thus reduces the contrast of the image. This process is known as attenuation. The scattered light beams play the role of an infinite number of tiny light sources floating in the atmosphere. These particles are responsible for unwanted whiteness observed in the scene, and hence, the airlight is mainly because of these light sources. In the existing literature, an airlight map is also considered a function of the distance of the scene from the camera [19]. In an outdoor environment, the depths are varied for different objects, and thus the airlight should be different for all these objects in the scene. The airlight map must be smooth except at the edges of the scene. Therefore, a similar type of anisotropic diffusion model can be used to correct airlight map degraded by the fog. Moreover, the process of removing fog from a single image is a challenging task due to its ill-posed nature. Before applying restoration process, its model must be analyzed for the well-posedness.

In recent past, several algorithms were given for restoring the fog affected images. The first category of models was based on the simple image enhancement techniques to restore the foggy images [16]. The enhancement achieved by such algorithms were found limited. Moreover, it required multiple images of the same scene under the same weather conditions. The second category of the algorithms was based on the use of polarization filters to remove the fog effect from the images [22, 23]. In this class of methods, the depth of the scene was restored using the polarization property of scattered light from multiple images captured with varying degrees of polarization. In [19], the algorithm makes use of the multiple reference images of the scene in bright weather condition. Therefore, such a method needs a particular imaging sensor to build a database of reference images under the same weather conditions. It was one of the drawbacks of these methods for not befitting in real-time applications.

The methods related to single image fog removal depend on the characteristics and textural information of the original (fog-free) image. In [25], the algorithm maximizes the local contrast of the image using Markov-Random-Field (MRF) model. The results were found impressive except few blocking artifacts around the depth discontinuities (edges). The algorithm proposed in [5] used Independent Component Analysis (ICA). The results obtained with this ICA-based approach were found satisfactory. However, an issue related to the computational complexity was noticed. In the third category of the algorithms, Dark-Channel-Prior(DCP) was used to address the defogging of images. Mainly, DCP depends on the statistics of the images of an outdoor scene [8]. Such images use to have at least one color channel in which pixels have intensities that are very low or close to zero and termed them *dark-pixels*. In the presence of fog, the intensities of these dark pixels rise due to the airlight artifact. Therefore correction of DCP results in the restoration of the fog affected image. Several models were proposed by making use of DCP-based restoration of the airlight map those include [6, 29] etc. The paper [24] lists a good review of the existing fog removal algorithms. Recently, few algorithms use learnable filters to design governing PDEs and associated boundary conditions [2, 17, 18]. These approaches are data-driven and contain very few manually chosen parameters.

In this study, the proposed algorithm corrects the airlight map by using a fractional order anisotropic diffusion (Fr-AD) process. The Fr-AD algorithm is a generalization of classical anisotropic diffusion (AD) [27]. Also, it is a pseudo-PDE-based algorithm between

Perona-Malik model and fourth-order anisotropic diffusion equations [32]. However, use of fractional anisotropic diffusion is made first time to the best of our knowledge for restoring foggy images. The computations of the fractional derivatives are carried out in the spatial domain instead of the existing Fourier domain-based methods [11]. Additionally, very few parameters are selected manually in the proposed algorithm. These manually tuned parameters do not depend on the image under restoration and remain fixed. The iterative algorithm takes the initial airlight map as the input, and then subsequent iterations derive towards the refined airlight map. The convergence analysis is carried out of the numerical scheme. The presented numerical results validate the better performance of the Fr-AD over some of the existing algorithms.

2 Preliminaries

2.1 Fractional order derivative

Let $f(z)$ be an analytic function in a simple connected region of the complex z- plane $\mathbb{C}$ containing origin. The fractional integral $I_z^{\alpha} f(z)$ of an order α of the function $f(z)$ is defined in [30]. The generalization of the fractional integral can be determined by taking into account the natural $n \in \mathbb{N}$ and real μ in the n-fold integral, and then operating the Cauchy's formula for iterated kernel's $n-1$ times. With this process, the fractional integral operator is given by

$$I_z^{\alpha,\mu} f(z) = \frac{(\mu+1)^{1-\alpha}}{\Gamma(\alpha)} \int_0^z (z^{\mu+1} - \xi^{\mu+1})^{\alpha-1} \xi^{\mu} f(\xi) d\xi. \tag{1}$$

where $\alpha, \mu(\neq -1) \in \mathbb{R}$.

When $\mu = 0$, we get the classic Riemann-Liouville fractional integral. Further, we will define Riemann-Liouville fractional derivatives using this fractional integral.

The generalized differential operator of order α resembling to the generalized fractional integral is defined in the subsequent manner:

$$D_z^{\alpha,\mu} f(z) = \frac{(\mu+1)^{\alpha}}{\Gamma(1-\alpha)} \frac{d}{dz} \int_0^z \frac{\xi^{\mu}}{(z^{\mu+1} - \xi^{\mu+1})^{\alpha}} f(\xi) d\xi, \quad 0 \leq \alpha < 1 \tag{2}$$

$$D_z^{\alpha} f(z) = \frac{d}{dz} \left(\frac{z^{-\alpha}}{\Gamma(1-\alpha)} * f(z) \right) = \frac{d}{dz} \left(\frac{z^{-\alpha}}{\Gamma(1-\alpha)} \right) * f(z) \tag{3}$$

The partial fractional derivatives with respect to x and y variables are calculated by convoluting the initial airlight map with fixed small size matrices $\begin{bmatrix} -1 & 1 \\ -1 & 1 \end{bmatrix}$ and $\begin{bmatrix} -1 & -1 \\ 1 & 1 \end{bmatrix}$ respectively weighted by using α and a constant viz. 0.25. The derivatives keep refining as per the refinement in airlight map with increasing iterations. The convolution method we followed returns the central part of the convolution that is the same size of the airlight map. Figure 1 illustrates the norm of the gradient vector for different fractional orders.

2.2 Anisotropic diffusion

Images consist of structures with a large collection of scales. Many times it is not known prior that which scale is suitable for the described information. Therefore, it is needed to model the image at different scales. In 1990, Perona and Malik introduced anisotropic diffusion [20] which simulates the process that generates scale space. Anisotropic diffusion is a

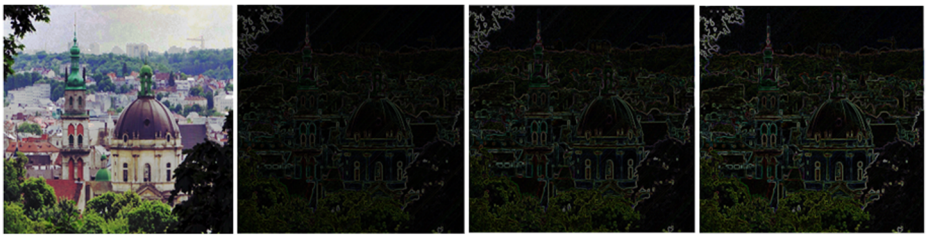

Fig. 1 Norm of derivatives in x and y direction on initial airlight map of Tomb image for: (**b**) $\alpha = 1$; (**c**) $\alpha = 1.4$; (**d**) $\alpha = 1.8$

generalization of the linear diffusion (heat equation). Perona-Malik model diffuses the intra-region prohibiting cross region boundaries in the images. Mathematically, linear anisotropic diffusion (in divergence form) is given as the following elliptic PDE

$$\partial_t u = div(\mathbf{D}\nabla u) \tag{4}$$

where, div is the divergence operator, and ∇ is the gradient operator. Here, $\mathbf{D}$ is a collection of symmetric and positive definite diffusion tensors. The above equation is complimented with an initial condition as $u(\mathbf{x}, 0) = u_0$, and the Neumann's type boundary conditions [28]. If we consider $D = I_d$, the d-dimensional identity diffusion tensor, then the above equation is converted into standard heat equation. The standard heat equation is appropriate to remove the artifacts like noise and fog from the image. However, it blurs the sharp details of the output image.

In the nonlinear anisotropic diffusion, the diffusion tensor $\mathbf{D}$ is defined in terms of the filtered image u. Mathematically, the equation for nonlinear anisotropic diffusion is given as

$$\partial_t u = div(\mathbf{D}_u \nabla u)$$

together with again an initial and Neumann's type boundary conditions. In [20], following tensors were used to define the above nonlinear anisotropic diffusion equation

$$\mathbf{D}_u(x,t) = c_u(x,t) I_d \qquad \text{with} \qquad c_u(x,t) = \frac{1}{\sqrt{1 + \|\nabla u(x,t)\|^2 \lambda^{-2}}}$$

where $\lambda > 0$ is a user specified constant. The above equation reveals that the filtering (smooth) will act with high impact in the uniform region, however it will be having weak impact when the gradient ∇u is having higher response, i.e. near and on the edges (boundaries of the uniform regions). This avoids the presence of blurry edges in the output image.

3 Proposed algorithm

3.1 Model description

An illustration of the proposed algorithm is given in Fig. 2. In the existing literature, several models have been proposed for the image with foggy information [19, 22, 26]. However, the most general model to describe an image degraded with fog effect can be expressed as

$$I(x, y) = I_0(x, y)e^{-kd(x,y)} + I_\infty(1 - e^{-kd(x,y)}) \tag{5}$$

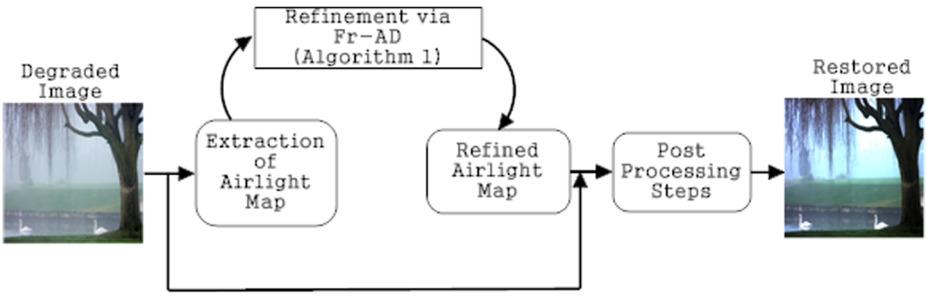

Fig. 2 An illustration of the proposed algorithm

where $I_0(x, y)$ is the original image (intensity at pixel location (x, y) in the absence of fog), k is the coefficient of the scattering related to the atmosphere and $d(x, y)$ is the distance of the scene from camera. The array I_∞ is atmospheric light or sky intensity and $I(x, y)$ is the observed foggy image of the scene. Here, $e^{-kd(x,y)}$ is often represented as transmission map and is given by $t(x, y) = e^{-kd(x,y)}$. In clear weather conditions, we have $k \approx 0$. However, k becomes non-negligible in foggy images. In (5), the first term $I_0(x, y)e^{-kd(x,y)}$ is referred as direct attenuation and second term $I_\infty(1 - e^{-kd(x,y)})$ is the airlight map. The decay of the scene radiance in the medium is occurred due to the presence of this direct attenuation term. Generally, scene color is changed due to the diversion in the airlight map. Attenuation is an decreasing function at an exponential rate. This reduces the contrast of the scene. The airlight map $A(x, y)$ produces whiteness in the scene. The (5) can be modified as

$$I(x, y) = I_0(x, y)\left(1 - \frac{A(x, y)}{I_\infty}\right) + A(x, y) \tag{6}$$

Normalization is performed on foggy image for simulation. As effect of the fog is pure white so the sky intensity may be taken as 1 throughout the array, and hence, (6) becomes

$$I(x, y) = I_0(x, y)(1 - A(x, y)) + A(x, y) \tag{7}$$

To restore $I_0(x, y)$ from its degraded version $I(x, y)$, we need to estimate $A(x, y)$ accurately. The airlight map $A(x, y)$ is a positive scalar map. Generally, outdoor images are colorful(contains trees, purple red plants and blue water), hence, the assumption of using DCP is true in case of natural images.

3.2 Implementation

In general, smoothing is considered as one of the impressive technique that has been used in several applications related to restoration and enhancement of images. Here, our objective is to find a more refined/enhanced airlight map $\widehat{A}(x, y)$, so that the foggy image can be restored using this in the (7). If we perform traditional smoothing filtering approach on $A(x, y)$ in order to get $\widehat{A}(x, y)$, it can contaminate the image features like lines, edges and textures from this initial airlight map. In order to evade the damage, smoothing has to be robustly controlled by the extent of smoothing and direction of smoothing. Anisotropic diffusion theory proposed by Perona and Malik [20] is a classical example of adaptive smoothing, where smoothing process is defined by PDEs. However, in this paper we generalize it to fractional order as the novelty. To do this, fractional order derivatives are included

instead of general integer order derivatives. Let c be the diffusion constant and t denotes the time, the anisotropic diffusion is presented as

$$\partial_t A = div(c(\nabla A)\nabla A) \tag{8}$$

The (8) is associated with the energy functional:

$$\mathrm{E}(A) = \int_{\Omega} f(|\nabla A|)d\Omega \tag{9}$$

where Ω stands for image support and $f(.) \geq 0$ is an increasing function associated with the diffusion coefficient defined as

$$c(s^2) = \frac{f'(s)}{s^2} \tag{10}$$

Anisotropic diffusion is presented as an energy consuming function that explore for the energy functional minimum. We consider the following functional defined in the space of continuous images over a support of Ω

$$\mathrm{E}(A) = \int_{\Omega} f(|\mathrm{D}^{\alpha} A|)d\Omega \tag{11}$$

where D^{α} is the fractional derivative operator defined as $\mathrm{D}^{\alpha} A = (\mathrm{D}_x^{\alpha} A, \mathrm{D}_y^{\alpha} A)$ and $|\mathrm{D}^{\alpha} A| = \sqrt{(\mathrm{D}_x^{\alpha})^2 + (\mathrm{D}_y^{\alpha})^2}$. We can compute the Euler-Lagrange equation for this minimization problem as follows:

Take any test function $\eta \in \mathcal{C}^{\infty}(\Omega)$. Define

$$\Phi(a) = \int_{\Omega} f(|\mathrm{D}^{\alpha} A + a\mathrm{D}^{\alpha}\eta|)dxdy \tag{12}$$

We obtain

$$\begin{aligned}
\Phi'(0) &= \frac{d}{da}\int_{\Omega} f(|\mathrm{D}^{\alpha} A + a\mathrm{D}^{\alpha}\eta|)dxdy \mid_{a=0} \\
&= \int_{\Omega}\left(f'(|\mathrm{D}^{\alpha} A|)\frac{\mathrm{D}_x^{\alpha} A}{|\mathrm{D}^{\alpha} A|}\mathrm{D}_x^{\alpha}\eta \right. \\
&\qquad \left. + f'(|\mathrm{D}^{\alpha} A|)\frac{\mathrm{D}_y^{\alpha} A}{|\mathrm{D}^{\alpha} A|}\mathrm{D}_y^{\alpha}\eta\right)dxdy \\
&= \int_{\Omega}((\mathrm{D}_x^{\alpha})^*(c(|\mathrm{D}^{\alpha} A|^2)\mathrm{D}_x^{\alpha} A) \\
&\quad + (\mathrm{D}_y^{\alpha})^*(c(|\mathrm{D}^{\alpha} A|^2)\mathrm{D}_y^{\alpha} A))\eta dxdy
\end{aligned} \tag{13}$$

for all $\eta \in \mathcal{C}^{\infty}(\Omega)$, where $(\mathrm{D}_x^{\alpha})^*$ and $(\mathrm{D}_y^{\alpha})^*$ are adjoint of D_x^{α} and D_y^{α}, respectively. Hence, the Euler-Lagrange equation becomes

$$(\mathrm{D}_x^{\alpha})^*(c(|\mathrm{D}^{\alpha} A|^2)\mathrm{D}_x^{\alpha} A) + (\mathrm{D}_y^{\alpha})^*(c(|\mathrm{D}^{\alpha} A|^2)\mathrm{D}_y^{\alpha} A) = 0 \tag{14}$$

The Euler-Lagrange equation can be solved using the following gradient descent method:

$$\partial_t A = -(\mathrm{D}_x^{\alpha})^*(c(|\mathrm{D}^{\alpha} A|^2)\mathrm{D}_x^{\alpha} A) - (\mathrm{D}_y^{\alpha})^*(c(|\mathrm{D}^{\alpha} A|^2)\mathrm{D}_y^{\alpha} A) \tag{15}$$

taking initial condition as the observed image $A(x, y)$. The solution is reached as $t \to \infty$ but the growth time can be stopped prior to attain the optimal trade off between fog removal and edge preservation.

When $\alpha = 1$, the (14) is absolutely the Perona-Malik (8); when $\alpha = 2$ (14) is absolutely the fourth order anisotropic diffusion in [32]; when $1 \leq \alpha \leq 2$, (14) leads to a "natural interpolation" between them.

3.3 Numerical algorithm

For practical applications, firstly assume that initial discrete image A is of $m \times m$ pixels. It has been sampled from its continuous version at uniformly spaced points starting at (0, 0), i.e. $A(x, y) = A(x\Delta x, y\Delta y)$ for $x, y = 0, ..., m-1$. The grid size Δx and Δy is chosen as $\Delta x, \Delta y = 1$.

Let K_1 and K_2 be purely diagonal operators in the spatial domain, defined by

$$\mathrm{K}_1 = \mathrm{F}^{-1}\big(diag\left(\left(1 - exp(-j2\pi(\omega_1)/m)\right)^{\alpha} \times exp(j\pi\alpha\omega_1/m)\right)\big)$$

$$\mathrm{K}_2 = \mathrm{F}^{-1}\big(diag\left(\left(1 - exp(-j2\pi(\omega_2)/m)\right)^{\alpha} \times exp(j\pi\alpha\omega_2/m)\right)\big)$$

where,

$$\mathrm{K}_1^* = \mathrm{F}^{-1}\big(diag\left(conj\left(\left(1 - exp(-j2\pi(\omega_1)/m)\right)^{\alpha} \times exp(j\pi\alpha\omega_1/m)\right)\right)\big), \tag{16}$$

and

$$\mathrm{K}_2^* = \mathrm{F}^{-1}\big(diag\left(conj\left(\left(1 - exp(-j2\pi(\omega_2)/m)\right)^{\alpha} \times exp(j\pi\alpha\omega_2/m)\right)\right)\big). \tag{17}$$

We compute the evolution of the initial image A , along flow (14) work in the spatial domain only. Moreover, we define

$$h_{xn} = c\left(|\mathrm{D}^{\alpha} A_n|^2\right) \mathrm{D}_x^{\alpha} A_n \tag{18}$$

and

$$h_{yn} = c\left(|\mathrm{D}^{\alpha} A_n|^2\right) \mathrm{D}_y^{\alpha} A_n \tag{19}$$

To summarize, our fog removal approach is done in following steps.

Algorithm 1 Numerical implementation of the Fr-AD

Input: Initial airlight map $A(x, y)$, maximum number of iterations n_{max}, α and $\Delta t = 4^{-\alpha}$
Output: Refined airlight map $\widehat{A}(x, y)$

1. **Set** $n = 0$, input image $u_0 = A(x, y)$, n_{max} and $t = k\Delta t$.
   for $n = 0, 1, 2, \ldots, n_{max}$, **do**
2. Compute $\tilde{\mathrm{D}}_x^{\alpha} u_n$ and $\tilde{\mathrm{D}}_y^{\alpha} u_n$ using (3).
3. Compute $h_{xn} = c\left(|\mathrm{D}^{\alpha} u_n|^2\right) \mathrm{D}_x^{\alpha} u_n$ and $h_{yn} = c\left(|\mathrm{D}^{\alpha} u_n|^2\right) \mathrm{D}_y^{\alpha} u_n$ as defined in (18) and (19).
4. Compute $g_n = \mathrm{K}_1^* \circ h_{xn} + \mathrm{K}_2^* \circ h_{yn}$
5. Compute $u_{n+1} = u_n - g_n \times \Delta t$
   End for
6. **return** $\widehat{A}(x, y) = u_n$

3.4 Analysis

The iterative scheme defined in the previous section needs to be converged for getting an enhanced airlight map $u = \widehat{A}(x, y)$. In this subsection, we briefly describe the convergence analysis of the scheme. The scheme defined in the Algorithm 1 converges for any choice of the initial image, if the energy function $f(|\nabla^{\alpha} u|)$ defined in (11) is smooth and convex [21]. Alternatively, there exists a unique solution of the diffusion PDE given in (14) if energy

function defined in (11) is smooth and convex. From [31],the eigenvalues of the Hessian matrix of the energy function $f(|\nabla^{\alpha}u|)$ can be written as

$$\lambda_1 = \frac{f'(|\nabla^{\alpha}u|)}{|\nabla^{\alpha}u|} \qquad \text{and} \qquad \lambda_2 = f''(|\nabla^{\alpha}u|) \tag{20}$$

This gives $\lambda_1 = c(.)$. Here, the value of λ_1 is positive due to our choice of the function $c(s^2) = s^{-1}$, since $f'(s) = s^2.c(s^2)$. To make the anisotropic diffusion problem as a well-posed, the value of second eigenvalue of the hessian matrix is quite important. In this scheme, we have

$$\lambda_2 = \frac{d}{ds}f'(s) = f''(s) = 1 > 0$$

due to the choice of the edge preserving function $c(s)$. This indicates that the Hessian matrix associated with the integrand of energy function f is positive definite and hence the function is strictly convex. In this case, the function f attains a unique global minima for any choice of initial image $u_0 = A(x, y)$ which is the airlight map extracted from the degraded image.

3.5 Post-processing

After estimating airlight map $\widehat{A}$ then de-foggy image $I_0(x, y)$ can be restored as

$$I_0(x, y, c) = \frac{(I(x, y, c) - \widehat{A}(x, y))}{(1 - (\widehat{A}(x, y)/I_{\infty}(c)))} \tag{21}$$

where $c \in (r, g, b)$. The above method can also be applied for gray-scale images. The only difference will be the initial airlight map.

Histogram stretching is applied as a post-processing step of the proposed algorithm. The restored image $I_0(x, y, c)$ obtained from the improved airlight map may be of poor contrast. Thus, the restored image may be visually dim because of the difference in the brightness of the scene radiance and the atmospheric light. The later one finds a bit brighter. In general, histogram equalization is a favorite technique for contrast enhancement. However, it may not be that worthy due to the saturated output image of the fog removal step. Moreover, histogram specification technique cannot be applied due to the absence of a standard reference image. Here, we adopted the histogram stretching in our algorithm for the task of contrast enhancement.

4 Results and discussions

This section presents the numerical results obtained with the proposed algorithm to enhance the digital images degraded by the fog effect. The proposed algorithm tests the performance on seven different images, namely Forest, Wheat, Tomb, Ny17, Swan, N6 and Train. These images are having different textural details and degraded with varying amount of the fog. In this study, the fractional order parameter α takes a real value in the interval $[1, 2)$. For the computational purpose, we choose five fixed values of $\alpha = \{1.0, 1.2, 1.4, 1.6, 1.8\}$ as taken in many references [1]. It is worth to mention that at $\alpha = 1$, the proposed scheme behaves similarly to AD scheme [27]. In existing literature, different strategies were adopted to stop the iterative process of anisotropic diffusion. We follow the stopping criteria as in [1]. Four different metrics *contrast gain (CG), colorfulness index (CI)*, *contrast-to-noise ratio*

Table 1 Details of the metrics used for quantitative analysis in this study

Metric	Description	Computational process
Contrast Gain (CG)	It is defined as the difference between mean contrasts of the degraded and recovered images. Due to the high contrast of the atmospheric light, an image is visually more clear and having better contrast than an image captured in foggy environment. Therefore, contrast gain is considered directly proportional to the accuracy of the proposed algorithm, i.e. better output will be having a higher value of contrast gain.	If the mean contrasts of the degraded and recovered images are given by $\bar{C}_{I_f}$ and $\bar{C}_{I_r}$, respectively, then the contrast gain in the restoration process is defined as $$CG = \bar{C}_{I_r} - \bar{C}_{I_f}$$ where, the contrast of a pixel is the ratio $C(x, y) = \frac{s(x,y)}{m(x,y)}$ with $$m(x, y) = \frac{1}{(2p+1)^2} \times \sum_{k=-p}^{p} \sum_{l=-p}^{p} I(x+k, y+l)$$ $$s(x, y) = \frac{1}{(2p+1)^2} \times \sum_{k=-p}^{p} \sum_{l=-p}^{p} \times |I(x+k, y+l) - m(x, y)|$$
Colorfulness Index (CI)	It estimates the quality of the color in the recovered image. In general, the images degraded by the fog are likely to have more whiteness which results as the less CI value. Thus, the CI value of a restored image must be higher than its degraded version.	The CI value of a RGB image $I(x, y)$ (having I_R, I_G and I_B bands) is computed as $$CI = \sqrt{\sigma_{I_1}^2 + \sigma_{I_2}^2} + 0.3\sqrt{\mu_{I_1}^2 + \mu_{I_2}^2}$$ where σ and μ denotes the standard deviation and mean of an image, respectively. The images $I_1 = I_R - I_G$ and $I_2 = \frac{1}{2}[I_R + I_G - I_B]$ are computed using color bands of $I(x, y)$.
Contrast-to-Noise ratio (CNR)	In the image restoration applications like fog removal, signal-to-noise ratio may not be considered as a good measure. An alternate of this is contrast-to-noise ratio (CNR). CNR is similar to the metric, signal-to-noise ratio (SNR), but subtracts off a term before taking the ratio. This is important when there is a significant bias in an image, such as from fog or haze.	Mathematically, it is defined as $$CNR = \frac{|S_A - S_B|}{\sigma_N}$$ where S_A and S_B are signal intensities for the signal structure A and B, respectively; and σ_N is the standard deviation of the image noise [12]. Here, we list the differences of CNR values between the foggy image and restored image in Tables 4 and 6.
Visible edges ratio (VER)	The ratio of visible edges is defined as $$e = \frac{n_l - n_k}{n_l} \quad (22)$$ where n_k and n_l are the cardinalities of visible edges in the foggy image and the fog free image respectively. Thus, higher value of e shows the better edge preservation.	We use an algorithm proposed in [24] for computing the visible edges ratio.

Table 2 Contrast gain (CG) obtained with the proposed algorithm with different fractional orders α with 30 iterations as stopping criteria

$\alpha =$	**1.0**	**1.2**	**1.4**	**1.6**	**1.8**
Forest	0.1078	0.1082	**0.1086**	0.1084	**0.1086**
Wheat	0.0852	0.0853	0.0854	0.0854	**0.0856**
Tomb	0.0891	**0.0897**	0.0896	0.0895	0.0893
Ny17	0.1347	0.1351	**0.1352**	0.1351	0.1350
Swan	0.0752	0.0753	0.0753	0.0753	**0.0754**
N6	0.0729	0.0732	0.0734	0.0734	**0.0735**
Train	0.1064	0.1067	**0.1069**	**0.1069**	0.1065

(CNR) and *visible edges ratio (VER)* are used to measure the performance of the proposed algorithm (See Table 1). The stopping criterion is chosen to be 30 iterations of the diffusion process based on all these metrics. The proposed algorithm uses the airlight map extracted from the degraded image as the initial image of the diffusion process. We compare the performance of the proposed algorithm with some of the existing algorithms such as DCP-based approach [8], Kernel regression model with DCP [29], Two-Layer Gaussian process regression (GPR) [4] and Integer order AD [27].

Table 2 lists the numerical results in terms of contrast gain (CG). In case of *Wheat*, *Swan* and *N6* images, fractional order $\alpha = 1.8$ gives the best CG value. For *Forest*, *Ny17* and *Train* images, $\alpha = 1.4$ is giving a slight better CG value. For *Tomb* image, the best CG value is obtained at $\alpha = 1.2$. It is also worth to mention that the results are significantly improved with fractional orders as compared to the case of $\alpha = 1$ (AD [27]).

The numerical results in terms of colorfulness index (CI) are listed in Table 3. The best CI values for all the images are obtained for the fractional orders $\alpha = 1.6$ & 1.8. This is due to the textural details of the image. Unlike the CG value, best CI values are obtained with $\alpha = 1.6$ for *Forest* and *Wheat* images. For rest of the images, the best performance is found at $\alpha = 1.8$. However, in all the these images, Fr-AD gives better results when compared to the AD.

Similar type of results are obtained in case of contrast-to-noise ratio. Table 4 lists the values of CNR at different fractional orders in case of all these images. It is noticeable that the best results are obtained with fractional orders and not with $\alpha = 1.0$. It is also noticeable from Table 5 that the Fr-AD based approach gives better visible edges ratio (VER) than the AD. From these observations, the significance of fractional order derivatives in anisotropic diffusion can be observed especially in the restoration of fog affected images.

Table 3 Colorfulness index (CI) value obtained with the proposed algorithm with different fractional orders α with 30 iterations as stopping criteria

$\alpha =$	**1.0**	**1.2**	**1.4**	**1.6**	**1.8**
Forest	0.1178	0.1188	0.1191	**0.1192**	**0.1192**
Wheat	0.0901	0.0905	0.0906	**0.0907**	**0.0907**
Tomb	0.1340	0.1349	0.1351	0.1351	**0.1352**
Ny17	0.4085	0.4122	0.4136	0.4141	**0.4142**
Swan	0.2394	0.2410	0.2416	0.2418	**0.2419**
N6	0.1628	0.1643	0.1648	0.1650	**0.1651**
Train	0.2901	0.2931	0.2941	0.2944	**0.2945**

Table 4 Contrast-to-noise ratio (CNR) obtained with the proposed algorithm with different fractional orders α with 30 iterations as stopping criteria

$\alpha =$	**1.0**	**1.2**	**1.4**	**1.6**	**1.8**
Forest	19.9636	20.1646	22.1766	23.1968	**24.2256**
Wheat	5.6686	5.9215	6.8548	7.7767	**7.8552**
Tomb	6.0246	7.0256	7.0657	7.0689	**7.0805**
Ny17	5.5305	6.1981	6.2973	6.4577	**6.5920**
Swan	7.8502	8.1070	8.2166	8.4867	**8.6664**
N6	24.1493	25.1423	25.1987	25.2607	**25.3376**
Train	10.1965	10.5583	10.6444	10.7655	**10.8092**

The performance of the proposed algorithm is compared with four different algorithms. Table 6 lists the results of this comparison study. We make the following remarks based on this comparison study.

1. In case of contrast gain, the proposed algorithm performs better than other all the four algorithms for *Forest* and *Tomb* images. The DCP algorithm performs better than the proposed algorithm in case of rest images. For *Ny17, Swan* and *Train* images, the proposed algorithm performs better than the three algorithms KRM, GPR and AD.
2. The proposed algorithm performs better in case of colorfulness index for *Ny17, Swan* and *Train* images. The KRM algorithm performs better than all algorithms for *Forest*, *Tomb* and *N6* images. The GPR algorithm performs best for *Wheat* image.
3. In case of metric CNR, the KRM algorithm performs better for *Tomb, Ny17* and *Swan* images. The proposed algorithm gives best results for *Forest, N6* and *Train* images. The GPR algorithm performs best for *Wheat* image. For *Swan* image, the proposed algorithm performs better than the three methods DCP, GPR and AD.
4. The proposed algorithm gives better VER value than DCP, KRM, GPR and AD for images *Forest*, *Swan* and *N6*. The KRM algorithm [29] performs better for other images. In case of visible edges ratio, the proposed algorithm performs better than the three methods DCP, GPR and AD for the images *Wheat, Tomb, Ny17* and *Train*.

Based on the overall comparison of the results, the proposed algorithm is a good choice to restore the foggy images. The computational time taken in the implementation of the proposed diffusion process is compared with a Fourier domain-based algorithm [1]. On a single processor, the proposed algorithm takes less than half of the computational time taken by other algorithms (See Table 7). In case of multi-chip, the Fourier domain based implementation may be a better choice.

Table 5 Visible edges ratio (VER) obtained with the proposed algorithm with different fractional orders α with 30 iterations as stopping criteria

$\alpha =$	**1.0**	**1.2**	**1.4**	**1.6**	**1.8**
Forest	0.2245	0.2308	0.2308	**0.2326**	0.2289
Wheat	0.2340	0.2372	0.2372	**0.2390**	0.2353
Tomb	0.0123	**0.0263**	**0.0263**	0.0170	0.0193
Ny17	0.1578	0.1586	**0.1609**	**0.1609**	**0.1609**
Swan	0.5390	0.5419	**0.5535**	0.5506	0.5506
N6	0.7825	**0.7899**	**0.7899**	**0.7899**	0.7895
Train	0.2061	0.2121	0.2121	**0.2239**	**0.2239**

Table 6 Comparison of the results obtained with existing algorithms DCP [8], KRM [29], GPR [4], AD [27] and the **proposed algorithm** (with α)

Metric	Algorithm	Forest	Wheat	Tomb	Ny17	Swan	N6	Train
CG	DCP	0.0567	**0.1628**	0.0635	**0.1989**	**0.1836**	**0.5418**	**0.3223**
	KRM	0.1040	0.1129	0.0756	0.1084	0.0637	0.0649	0.0967
	GPR	0.0218	0.0222	0.0824	0.1139	0.0561	0.0869	0.0623
	AD	0.1078	0.0852	0.0891	0.1347	0.0752	0.0729	0.1064
	Proposed	**0.1086**(1.8)	0.0856(1.8)	**0.0897**(1.2)	0.1352(1.4)	0.0754(1.8)	0.0735(1.8)	0.1069(1.6)
CI	DCP	0.1529	0.1470	0.1156	0.1029	0.0965	0.0774	0.0780
	KRM	**1.1639**	0.0736	**2.4508**	0.3255	0.2154	**3.1454**	0.1703
	GPR	0.0927	**0.1578**	0.1252	0.3753	0.1095	0.2269	0.2156
	AD	0.1178	0.0901	0.1340	0.4085	0.2394	0.1628	0.2901
	Proposed	0.1192(1.8)	0.0907(1.8)	0.1352(1.8)	**0.4142**(1.8)	**0.2419**(1.8)	0.1651(1.8)	**0.2945**(1.8)
CNR	DCP	12.4686	5.6009	10.5319	4.5410	5.7326	9.2940	6.4906
	KRM	11.7421	3.2639	**15.0357**	**12.5265**	**12.6067**	16.2957	7.2043
	GPR	23.2975	**9.6605**	2.4574	7.4326	7.9742	10.4769	8.4515
	AD	19.9636	5.6686	6.0246	5.5305	7.8502	24.1493	10.1965
	Proposed	**24.2256**(1.8)	7.8552(1.8)	7.0805(1.8)	6.5920(1.8)	8.6664(1.8)	**25.3376**(1.8)	**10.8092**(1.8)
VER	DCP	0.0152	0.0012	0.0042	0.0893	0.2857	0.0573	0.0283
	KRM	0.1870	**0.7134**	**0.1583**	**0.3397**	0.3486	0.3844	**0.2925**
	GPR	0.0730	0.0171	0.0040	0.0674	0.4297	0.2078	0.0261
	AD	0.2245	0.2340	0.0123	0.1578	0.5390	0.7825	0.2061
	Proposed	**0.2326**(1.6)	0.2390(1.6)	0.0263(1.2)	0.1609(1.8)	**0.5535**(1.4)	**0.7899**(1.2)	0.2239(1.8)

Table 7 Computational time (in seconds) obtained in Fourier domain and by the proposed algorithm in spatial domain

Image	Fourier domain [1]	Proposed(Spatial)
Forest(256 × 256)	2.986921	1.007776
Wheat(256 × 256)	2.861586	1.012766
Tomb(256 × 256)	2.936528	0.985334
Ny17(256 × 256)	2.850443	1.010316
Swan(256 × 256)	2.661488	0.896816
N6(256 × 256)	2.651796	0.895613
Train(256 × 256)	2.980296	1.048273

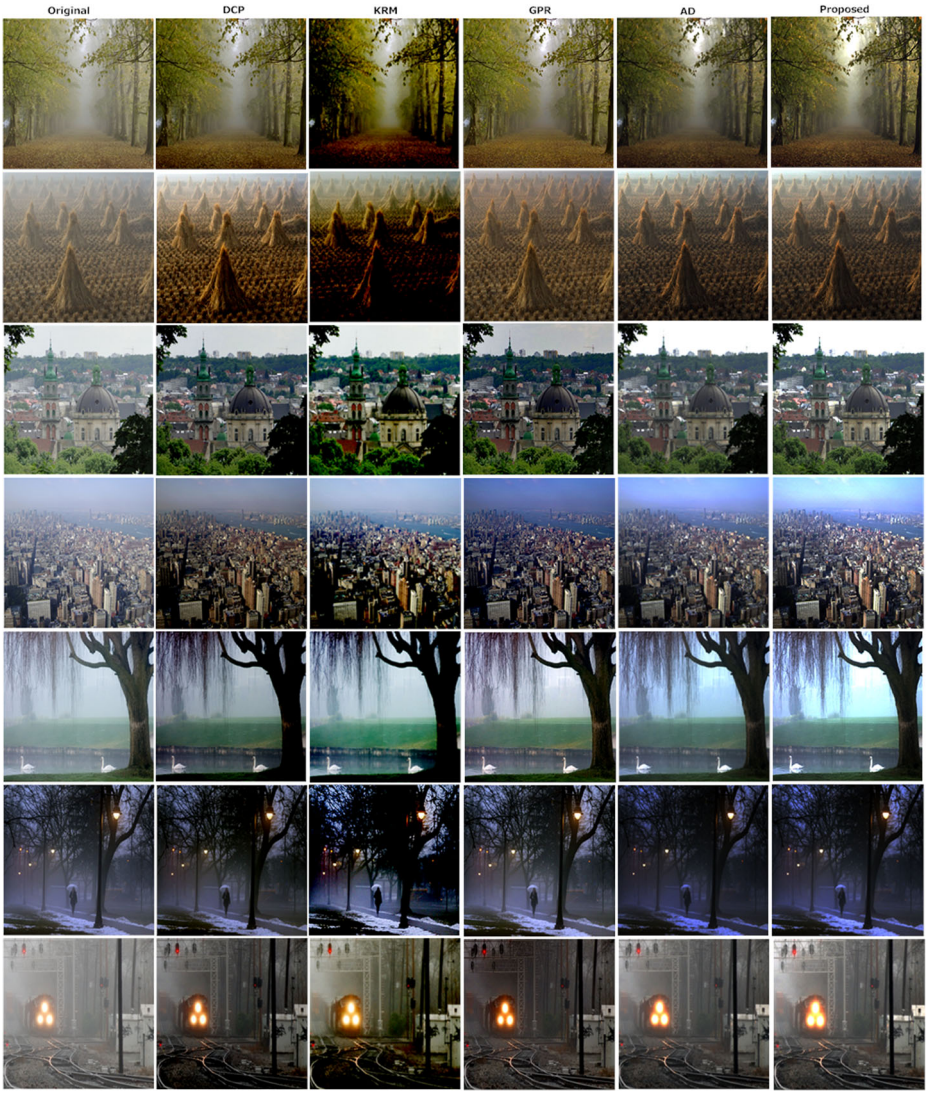

Fig. 3 The original foggy images are given in first column. Restored images with DCP [8], KRM [29], GPR [4], AD [27] and the proposed algorithm (at $\alpha = 1.8$) are shown in second, third, fourth, fifth columns and sixth columns, respectively

Figure 3 gives a qualitative representation of the results obtained with DCP, KRM, GPR, AD and the proposed algorithm. These qualitative results affirm that the restored images with the proposed algorithm are visibly better than other four existing algorithms. The results obtained with KRM algorithm [29] has a whiteness along the edges which is smooth in case of the results obtained with the proposed algorithm. Hence, this apparently makes the proposed algorithm a better choice for image restoration where the fog degrades the original images.

5 Conclusions

This paper addresses the issue of defogging of the digital images by using a fractional order generalization of the anisotropic diffusion. The quality of restored images in the proposed algorithm depends on the diffused airlight map. The proposed algorithm diffuses airlight map visually better when compared to classical anisotropic diffusion. The proposed algorithm gives restored images better than some of the benchmark algorithms based on different metrics. The computation of the fractional order derivatives in the proposed algorithm takes lower computational efforts when compared to a Fourier domain-based implementation. In this study, five fixed values between $[1,\ 2)$ are considered for computing fractional order derivatives. An adaptive choice of the fractional orders and use of learnable PDEs might be possible future directions to extend the proposed work.

Acknowledgements This work is partially supported by the Indian Space Research organization through their RESPOND scheme. One of the authors Savita Nandal is also thankful to Ministry of Human Resources and Development for financial support for carrying out her Ph.D. work.

References

1. Bai J, Feng XC (2007) Fractional-order anisotropic diffusion for image denoising. IEEE Trans Image Process 16(10):2492–2502
2. Chen Y, Pock T (2017) Trainable nonlinear reaction diffusion: a flexible framework for fast and effective image restoration. IEEE Trans Pattern Anal Mach Intell 39(6):1256–1272
3. Cheng G, Han J, Guo L, Qian X, Zhou P, Yao X, Hu X (2013) Object detection in remote sensing imagery using a discriminatively trained mixture model. ISPRS J Photogramm Remote Sens 85:32–43
4. Fan X, Wang Y, Tang X, Gao R, Luo Z (2017) Two-layer Gaussian process regression with example selection for image dehazing. IEEE Trans Circ Syst Video Technol 27(12):2505–2517
5. Fattal R (2008) Single image dehazing. In: Proceedings of ACM SIGGRAPH
6. Gibson KB, Vo DT, Nguyen TQ (2012) An investigation of dehazing effects on image and video coding. IEEE Trans Image Process 12(2):662–673
7. Han J, Zhang D, Cheng G, Guo L, Ren J (2015) Object detection in optical remote sensing images based on weakly supervised learning and high-level feature learning. IEEE Trans Geosci Remote Sens 53(6):3325–3337
8. He K, Sun J, Tang X (2011) Single image haze removal using dark channel prior. IEEE Trans Pattern Anal Mach Intell 33(12):2341–2353
9. He K, Sun J, Tang X (2013) Guided image filtering. IEEE Trans Pattern anal Mach Intell 35(6):1397–1409
10. Huang Y, Guan Y (2016) Laplacian hashing for fast large-scale image retrieval and its applications for midway processing in a cascaded face detection structure. Multimed Tools Appl 75(23):16315–16332

11. Janev M, Pilipovic S, Atanackovic T, Obradovic R, Ralevic N (2011) Fully fractional anisotropic diffusion for image denoising. Math Comput Model 54:729–741
12. Jiang H, Lu N, Yao L (2016) A high fidelity haze removal method based on HOT for visible remote sensing images. Remote Sens 8:844
13. Kamalaveni V, Veni S, Narayanankutty KA (2017) Improved self-snake based anisotropic diffusion model for edge preserving image denoising using structure tensor. Multimed Tools Appl 76(18):18815–18846
14. Karasulu B, Korukoglu S (2011) A software for performance evaluation and comparison of people detection and tracking methods in video processing. Multimed Tools Appl 55(3):677–723
15. Kermani E, Asemani D (2014) A robust adaptive algorithm of moving object detection for video surveillance. EURASIP J Image Video Process 2014(27):1–9
16. Kim TK, Paik JK, Kang BS (1998) Contrast enhancement system using spatially adaptive histogram equalization with temporal filtering. IEEE Trans Consum Electron 44(1):82–87
17. Liu R, Zhong G, Cao J, Lin Z, Shan S, Luo Z (2016) Learning to diffuse: a new perspective to design pdes for visual analysis. IEEE Trans Pattern Anal Mach Intell 38(12):2457–2471
18. Liu R, Fan X, Hou M, Jiang Z, Luo Z, Zhang L Learning Aggregated Transmission Propagation Networks for Haze Removal and Beyond, arXiv:1711.06787
19. Narasimhan SG, Nayar SK (2000) Chromatic framework for vision in bad weather. Proc IEEE Conf Comput Vis Pattern Recognit 1:598–605
20. Perona P, Malik J (1990) Scale-space and edge detection using anisotropic diffusion. IEEE Trans Pattern Anal Mach Intell 12(7):629–639
21. Prasath VBS, Singh A (2010) Multispectral image denoising by well-posed anisotropic diffusion scheme with channel coupling. Int J Remote Sens 31(8):2091–2099
22. Schechnner YY, Narasimhan SG (2001) Instant dehazing of images using polarization. In: Proceedings of IEEE computer society conference on computer vision and pattern recognition, CVPR. Kauai, pp 325–332
23. Schechnner YY, Narasimhan SG, Nayar SK (2003) Polarization-based vision through haze. Appl Opt 42(3):511–525
24. Singh D, Kumar V (2018) Comprehensive survey on haze removal techniques. Multimed Tools Appl 77(8):9595–9620
25. Tan RT (2008) Visibility in bad weather from a single image. In: Proceedings of IEEE conference on computer vision and pattern recognition, (CVPR), pp 1–8
26. Tarel J-P, Hautiere N (2009) Fast visibility restoration from a single color or gray level image. In: Proceedings of IEEE 12th international conference on computer vision (ICCV), pp 2201–2208
27. Tripathi AK, Mukhopadhyay S (2012) Single image fog removal using anisotropic diffusion. IET Image Process 6(7):966–975
28. Weickert J (1996) Theoretical foundations of anisotropic diffusion in image processing. Comput Suppl 11:221–236
29. Xie CH, Qiao WW, Liu Z, Ying WH (2017) Single image dehazing using kernel regression model and dark channel prior. SIViP 11(4):705–712
30. Yirenkyi PA, Appati JK, Dontwi IK (2016) A new construction of a fractional derivative mask for image edge analysis based on Riemann-Liouville fractional derivative. Advances in Difference Equations. Springer
31. You Y-L, Kaveh M, Xu W, Tannenbaum A (1994) Analysis and design of anisotropic diffusion for image processing. In: IEEE international conference of image processing. Austin, vol II, pp 497–501
32. You Y-L, Kaveh M (2000) Fourth-order partial differential equations for noise removal. IEEE Trans Image Process 9(10):1723–1730

Savita Nandal received the BSc degree from Maharshi Dayanand University in 2011, the MSc degree from Indian Institute of Technology, Roorkee in 2013, both in applied mathematics and is pursuing PhD degree in image processing from Indian Institute of Technology, Roorkee since 2014. Her current research interests includes Computer Vision/ Mathematical Image processing, Nonlinear Optimization and Machine Learning.

Sanjeev Kumar is working as an Associate Professor with Department of Mathematics, Indian Institute of Technology Roorkee since April 2016. Earlier, he worked as an assistant professor with Department of Mathematics, Indian Institute of Technology Roorkee from November 2010 to April 2016. He also worked as a postdoctoral fellow with Department of Mathematics and Computer Science, University of Udine, Italy from March 2008 to November 2010. He has completed his PhD in Applied Mathematics from IIT Roorkee, India in 2008. His areas of research include image processing, inverse problems and machine learning. He has co-convened the first international conference on computer vision and image processing in 2016, and has served as a reviewer and program committee member of more than 20 international journals and conferences. He conducted two workshops on Image Processing at IIT Roorkee in recent years. He has published more than 58 papers in various international journals and reputed conferences. He has completed a couple of sponsored research projects.